ACES Asian Chemical Editorial Society

doi.org/10.1002/cnma.202100258

CHEMNANOMAT
Full Paper

# Design of bimetallic Au/Cu nanoparticles in ionic liquids: Synthesis and catalytic properties in 5-(hydroxymethyl)furfural oxidation

Georgios Uzunidis,[a] Oliver Schade,[a, b] Dieter Schild,[c] Jan-Dierk Grunwaldt,[a, b] and Silke Behrens*[a]

**Abstract:** In alloyed nanoparticles, synergistic electronic and/or geometric effects may enhance the catalytic properties compared to their monometallic counterparts. Herein, we address the synthesis of bimetallic Au/Cu nanoparticles with different compositions by wet chemical reduction in ionic liquids. The nanoparticles were successively supported on carbon. The ionic liquid could be recycled after synthesis. Annealing of the carbon-supported NPs at 400 °C led to NPs of the ordered intermetallic $L1_0$ AuCu phase. The nanoparticle-derived catalysts were characterized by X-ray diffraction analysis, transmission electron microscopy, X-ray photoelectron spectroscopy and optical emission spectroscopy with inductively coupled plasma. Oxidation of biomass-derived furans is a prominent process for biomass transformation into value-added chemicals. Herein, the oxidation of 5-hydroxymethyl-2-furfural (HMF) to 2,5-furandicarboxylic acid (FDCA) was chosen as a model reaction to evaluate the effect of Cu addition and intermetallic structure on the catalytic performance. Particularly Au/Cu nanoparticles with an Au/Cu ratio of 3:1 showed very high conversion to FDCA.

## Introduction

Pre-Columbian civilizations in Central and South America already perfected gold-copper (Au/Cu) alloys, in particular for decorative arts, and they are still used today for jewelry.[1] Alloying these two coinage metals not only comes with a characteristic reddish tint and a congruent melting point but also ameliorates the instability of copper towards oxidation and pulls down the cost of gold. More recently, nanoscale Au/Cu phases have also emerged as important catalysts.[2] Such bimetallic catalysts have attracted considerable attention since they offer a way to tailor the catalytic properties of metals.[3] Synergistic electronic and/or geometric effects were shown to enhance the catalytic performance of bimetallic metal particles compared to their monometallic counterparts.[3c,4] Au/Cu nanoparticles (NPs) catalyze a wide range of chemical reactions ranging from oxygen reduction reaction,[5] oxidation of carbon monoxide, alcohols and aldehydes.[2,4a,6] Their catalytic properties depend on size, morphology, metal ratio, composition, and element distribution within the NPs.[3a,7]

The Au/Cu combination follows three of the four empirical Hume-Rothery rules to predict solid solubility: (1) small difference between the atomic radii (< 15%), (2) common crystal structures (face centered cubic, fcc) and (3) common valences (+1), but (4) their electronegativities are quite different (i.e., difference in Mulliken electronegativity values around 29%).[1] In the bulk, Au/Cu forms solid solutions (A1) at all compositions at high temperature while at lower temperatures well-ordered phases, $Au_3Cu$ ($L1_2$), AuCu ($L1_0$) and $AuCu_3$ ($L1_2$), occur depending on the composition (Figure 1).[8] A plethora of methods has been used to synthesize Au/Cu-based NPs and supported catalysts with stabilizers and conventional solvents, including co-reduction,[7c,9] and chemical deposition-precipitation procedures.[10] Recently, the synthesis of Au/Cu NPs was achieved for ultrasmall NP sizes (~2 nm) and a range of metal compositions (Au/Cu ratios 3:1, 1:1 and 1:3) by a modified Brust method.[11] NPs with ordered AuCu and $AuCu_3$ structure were synthesized *via* a seed-growth procedure employing Au seeds and high temperatures (280–300 °C).[12] Au/Cu NPs with cubic shape were received *via* a polyol process using complex

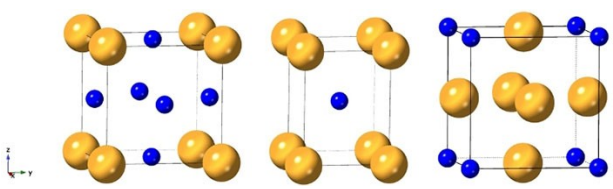

**Figure 1.** Schematic representation of the $AuCu_3$ ($L1_2$), AuCu ($L1_0$) and $Au_3Cu$ ($L1_2$) structure (Au: gold-colored, Cu: blue).

[a] G. Uzunidis, Dr. O. Schade, Prof. Dr. J.-D. Grunwaldt, Prof. Dr. S. Behrens
Institute of Catalysis Research and Technology
Karlsruhe Institute of Technology (KIT)
Hermann-von-Helmholtz-Platz 1,
76344 Eggenstein-Leopoldshafen (Germany)
E-mail: silke.behrens@kit.edu

[b] Dr. O. Schade, Prof. Dr. J.-D. Grunwaldt
Institute for Chemical Technology and Polymer Chemistry
Karlsruhe Institute of Technology (KIT)
Engesserstr. 20, 76131 Karlsruhe (Germany)

[c] Dr. D. Schild
Institute for Nuclear Waste Disposal
Karlsruhe Institute of Technology (KIT),
Hermann-von-Helmholtz-Platz 1, D-76344 Eggenstein-Leopoldshafen (Germany)

Supporting information for this article is available on the WWW under https://doi.org/10.1002/cnma.202100258

ligand mixtures (including 1-adamantanecarboxylic acid, 1-hexadecylamine, and 1-dodecanethiol).[13] Even the synthesis of pentacle-shaped Au/Cu NPs has been reported.[14] Typically, conventional NP synthesis requires use of strong capping agents to control NP size and shape and to stabilize the as-formed NPs.[15] However, capping agents can modify catalytic properties and even act as catalyst poison by electronic interface effects, sterically hindered access to catalytically active sites and selectively blocking of active sites on the NP surface.[16]

Room-temperature ionic liquids (ILs) reveal unique physicochemical properties (such as excellent solvent properties, low vapor pressure, high polarity, wide electrochemical stability window) and have received considerable attention as neoteric and tunable reaction media for NP synthesis. IL cations and anions are not only able to control NP formation processes but also prevent their aggregation *via* electrosteric stabilization, thus making the use of additional surfactants or ligands unnecessary.[17] Depending on the nature of the IL anions and cations, particles of different sizes and morphologies can be obtained.[18] ILs were exploited for the preparation of Au/Cu NPs by sputter-deposition techniques. For example, a library of binary Au/Cu alloy NPs was achieved by combinatorial sputtering into ILs contained in a cavity array wafer.[19] Intermetallic AuCu NPs were obtained *via* sputter-deposition in ILs and subsequent heat treatment.[20] To the best of our knowledge, however, ILs have not yet been exploited for the chemical synthesis of bimetallic Au/Cu NPs despite their well-known, beneficial properties for NP synthesis.

Oxidation of biomass-derived furans is a prominent process for biomass transformation into value-added chemicals and has been explored by various groups.[21] One of the most important products of HMF oxidation is 2,5-furandicarboxylic acid (FDCA) which has a huge prospective in the production of new bio-based polyesters and nylons and is considered as a promising alternative for terephthalic acid, which is widely used in polypropylene terephthalate (PET) and polybutylene terephthalate (PBT). HMF is successively oxidized to 5-hydroxymethyl-2-furancarboxylic acid (HFCA), 5-formyl-2-furancarboxylic acid (FFCA) and FDCA under most reaction conditions.[21a] Noble metals (such as Au, Pd, Pt or Ru) exhibit high activity and FDCA selectivity under mild reaction conditions with temperatures ranging from room temperature to 165 °C.[21a,22] Au particles supported on various materials (e.g. $ZrO_2$,[23] $TiO_2$,[24] C,[24] $CeO_2$,[25] $Ce_xZr_{1-x}O_2$[26]), for example, have been explored for the aerobic HMF oxidation. Bimetallic catalysts of Au such as Au/Cu catalysts were further shown to exhibit a higher FDCA yield with respect to their monometallic Au and Cu counterparts[9d][27] and are thus a good model reaction.

In this paper, we report on the synthesis of bimetallic Au/Cu NPs using a one-step reduction procedure and ILs as a reaction medium. The NPs were adsorbed on a carbon support and the IL was recycled for reuse in NP synthesis. The as-formed Au/Cu NPs initially revealed a random-type alloy structure (fcc, A1) and were subsequently annealed to form NPs with the intermetallic AuCu $L1_0$ structure. We have characterized the carbon-supported NPs for their size, metal loading, molar Au/Cu ratio, structure and oxidation state using electron microscopy (transmission electron microscopy (TEM) and scanning electron microscopy (SEM) with energy-dispersive X-ray spectroscopy (EDS)), powder X-ray diffraction (XRD), optical emission spectroscopy with inductively coupled plasma (ICP-OES), and X-ray photoelectron spectroscopy (XPS). The aerobic oxidation of 2,5-(hydroxymethyl)furfural (HMF) as a biomass-derived platform molecule was chosen as a model reaction to study the catalytic performance of the Au/Cu NPs and the effect of Cu addition.[6f,9c,d]

## Results and Discussion

In ILs, weakly coordinating anions and cations control both particle nucleation and growth processes.[4c,28] The IL anions and cations form semi-organized clusters which may provide protective layers for the electrosteric stabilization of NPs. We have previously shown that for different IL anions and cations NPs of different sizes and morphologies are obtained.[29]

Recently, we have also demonstrated the synthesis of intermetallic NPs in ILs by the simultaneous one-step co-reduction of the two metal precursors.[4c]

In this study, we employed three ILs with different types of cations and anions for NP synthesis. The used ILs [MMPyrr][FAP] and [BMPyrr][BTA] were chosen so that only one ion (i.e., for [MMPyrr][FAP] the cation, for [BMPyrr][BTA] the anion) differs from [BMPyrr][FAP], to study the effect caused by the anion and the cation on the size and composition of the NPs, respectively. The structures of the IL anions and cations are depicted in Figure 2.

For NP synthesis, the $HAuCl_4$ and $CuCl_2$ precursors were dispersed in the IL, followed by rapidly injecting the reducing agent, $Li[BEt_3H]$, while vigorously stirring. A change in color from brown to black indicated NP formation. The NPs were received as black suspension in the IL. In a next step, the Au/Cu NPs were immobilized on a carbon support by slowly adding

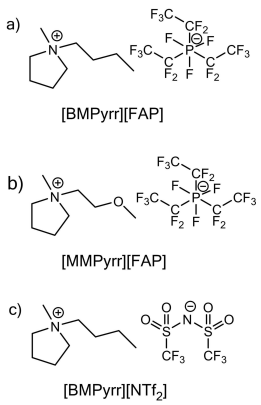


**Figure 2.** Structures of the ILs used herein for the synthesis of bimetallic Au/Cu NPs: a) 1-butyl-1-methylpyrrolidinium tris(pentafluorethyl) trifluorophosphate ([BMPyrr][FAP]), b) 1-(2-methoxyethyl)-1-methylpyrrolidinium tris-(pentafluorethyl) trifluorophosphate ([MMPyrr][FAP]), c) 1-butyl-1-methyl-pyrrolidinium bis(trifluoromethylsulfonyl)imide ([BMPyrr][$NTf_2$]).

the NPs to the carbon suspended in a THF/MeCN mixture. This destabilized the NPs in the IL and the Au/Cu NPs were adsorbed on the support material. The Au/Cu NP catalysts were isolated *via* centrifugation and the respective IL was recycled by subsequently washing with water, organic solvents and drying in vacuum. As demonstrated by NMR spectroscopy (Figure S8 in the Supporting Information (SI)), the recycled ILs were free of impurities and could be reused for NP synthesis providing an overall sustainable procedure for NP synthesis. Additionally, Au NPs 10 with a mean size of $5.2 \pm 2.0$ nm and 6.5 nm according to TEM and XRD analysis were synthesized in [BMPyrr][$NTf_2$] with the same procedure and used as a reference (Figure S1). ICP-OES analysis of the Au/Cu NP catalysts revealed metal loadings between 8 and 11 wt% (Table 1). The molar Au/Cu ratios were in good agreement with the initial molar ratio of the Au and Cu precursors.

Figure 3 shows representative TEM images of the carbon-supported Au/Cu NPs with different molar Au/Cu ratios. TEM images display small, spherical NPs which were homogeneously distributed over the carbon support. The size of the Au/Cu NPs was in the range of 3.3 and 4.7 nm with narrow size distribution (Table 1, Figure S2). For NPs synthesized in [MMPyrr][FAP], the NPs were partially agglomerated (Figure S3, see SI).

XRD analysis was employed to investigate the structure and phase composition of the NPs. The XRD diagrams of the bimetallic NPs with different Au/Cu ratios are shown in Figure 4. All XRD patterns reveal broad reflections of low intensity which are characteristic for small NPs. The crystallite size of the Au/Cu NPs was estimated using the Scherrer equation based on the full width at half maximum (FWHM) of the 111 reflection (Table 1). For all Au/Cu NP catalysts, the crystallite sizes according to the Scherrer equation were in a similar range as the mean NP sizes calculated based on TEM analysis (Table 1). The XRD patterns of the Au/Cu NPs (molar Au/Cu ratio 3:1 and 1:1) revealed four characteristic reflections of the fcc Au phase (A1) (Figure 4a and b). In comparison to the Au reference, the reflections of Au/Cu NPs seem to be slightly shifted to higher diffraction angles. In general, a shift of the reflections to higher diffraction angles is characteristic for a decrease of the lattice parameters by inserting Cu atoms into the Au lattice. The observed shift was small and may probably be also affected by XRD sample preparation. For the Cu-rich NPs (Au/Cu 1:1), the 111 reflections were clearly shifted to higher Bragg angles (i.e. 40.6° and 41.7° ($2\theta$) for synthesis in [MMPyrr][FAP] (AuCu–A1 NPs 5) and [BMPyrr][$NTf_2$] (AuCu–A1 NPs 8), respectively). For NP synthesis in [BMPyrr][FAP] (molar Au/Cu ratio 1:3, ($AuCu_3$–A1 NPs 3)), two maxima occurred at 38.5° and 43.1° for the 111 reflection which may indicate a segregation into Au-rich and Cu-rich NPs, respectively. For Au/Cu NPs synthesized at room temperature, the XRD patterns (Figure 4) did not reveal any characteristic reflections of the ordered intermetallic $Au_3Cu$ ($L1_2$), AuCu ($L1_0$) or $AuCu_3$ ($L1_2$) phase, suggesting a random distribution of Au and Cu in the NPs (A1 phase). Figure S5 compares the XRD diagrams of $Au_3Cu$, AuCu, and $AuCu_3$ NPs in each of the ILs.

In a next step, Au/Cu NPs with intermetallic structure were prepared by an additional annealing step. Initially, the synthesis of Au/Cu NPs with intermetallic structure was studied in the ILs by reducing the $HAuCl_4$ and $CuCl_2$ precursors (molar Au/Cu precursor ratio 1:1) with Li[$BEt_3H$] at room temperature, followed by an additional annealing step at 175 °C. This approach led to the formation of bimetallic Au/Cu-based NPs where the most intense reflections were in good agreement with the 101 and 110 reflections of the tetragonal AuCu phase, but SEM analysis revealed the formation of highly agglomerated Au/Cu particles (Figures S6 and S7 in the SI).

Therefore, the Au/Cu NPs (molar Au/Cu precursor ratio 1:1) were supported on carbon before the annealing step, placed in an ampoule, vacuum-sealed and successively annealed at 400 °C for 1 h.

Figure 5 shows the results of XRD analysis after annealing at 400 °C. In all cases, the reflections became narrower upon annealing at 400 °C. This indicated NP growth and was further confirmed by TEM analysis (Figure 6). The most prominent 101 and 110 reflections at 40.5° and 45.8° ($2\theta$) were in good agreement with tetragonal $L1_0$ AuCu phase.

Unlike the disordered Au/Cu NPs (molar Au/Cu ratio 1:1, Figure 4b) with fcc structure, the diagrams revealed additional reflections indicating the formation of the ordered tetragonal AuCu phase with $L1_0$ structure (e.g. the 100 and 002 reflections at 31.9° and 49.6° ($2\theta$)). TEM images (Figure 6) show AuCu NPs homogeneously dispersed over the carbon support. In addition, also a few larger NPs were formed by sintering processes (see Figure S4 in the SI). After annealing, the mean particle size

**Table 1.** Supported, bimetallic Au/Cu NP catalysts prepared with different Au/Cu ratios ($Au_3Cu$: 3:1; AuCu: 1:1 and $AuCu_3$: 1:3) and fcc structure (A1) in different ILs: Metal content (determined by ICP-OES), mean NP size (measured by TEM analysis) and crystallite size (estimated using the Scherrer equation).

| NPs | Catalyst | IL | Metal loading [wt%][a] | Au [wt%][a] | Cu [wt%][a] | Molar Au/Cu ratio | NP size[b] [nm] | Crystallite size[c] [nm] |
|---|---|---|---|---|---|---|---|---|
| **1** | $Au_3Cu$–A1 | [BMPyrr][FAP] | 10.3 | 9.4 | 0.9 | 77:23 | 3.5 (±0.9) | 4.3 |
| **2** | AuCu–A1 | [BMPyrr][FAP] | 8.7 | 6.5 | 2.2 | 49:51 | 3.9 (±0.9) | 2.8 |
| **3** | $AuCu_3$–A1 | [BMPyrr][FAP] | 8.3 | 4.3 | 4.0 | 26:74 | 3.8 (±1.2) | 2.4 |
| **4** | $Au_3Cu$–A1 | [MMPyrr][FAP] | 10.7 | 9.7 | 1.0 | 76:24 | 4.6 (±1.3) | 5.0 |
| **5** | AuCu–A1 | [MMPyrr][FAP] | 8.5 | 6.7 | 1.8 | 54:46 | 4.7 (±1.2) | 4.5 |
| **6** | $AuCu_3$–A1 | [MMPyrr][FAP] | 8.6 | 4.5 | 4.1 | 26:74 | 4.4 (±1.0) | 2.2 |
| **7** | $Au_3Cu$–A1 | [BMPyrr][$NTf_2$] | 11.1 | 10.1 | 1.0 | 77:23 | 4.3 (±1.1) | 5.2 |
| **8** | AuCu–A1 | [BMPyrr][$NTf_2$] | 8.5 | 6.7 | 1.8 | 54:46 | 4.5 (±1.4) | 3.1 |
| **9** | $AuCu_3$–A1 | [BMPyrr][$NTf_2$] | 8.4 | 4.4 | 4.0 | 26:74 | 3.3 (±0.8) | 4.4 |
| **10** | Au | [BMPyrr][$NTf_2$] | 7.0 | 7.0 | – | – | 5.2 (±2.0) | 6.5 |

[a] Determination of metal loading and metal content by ICP-OES. [b] Mean NP sizes were calculated from TEM images by measuring the size of at least 250 NPs. [c] Crystallite sizes were calculated using the Scherrer equation and the full width at half maximum (FWHM) of the 111 reflection.

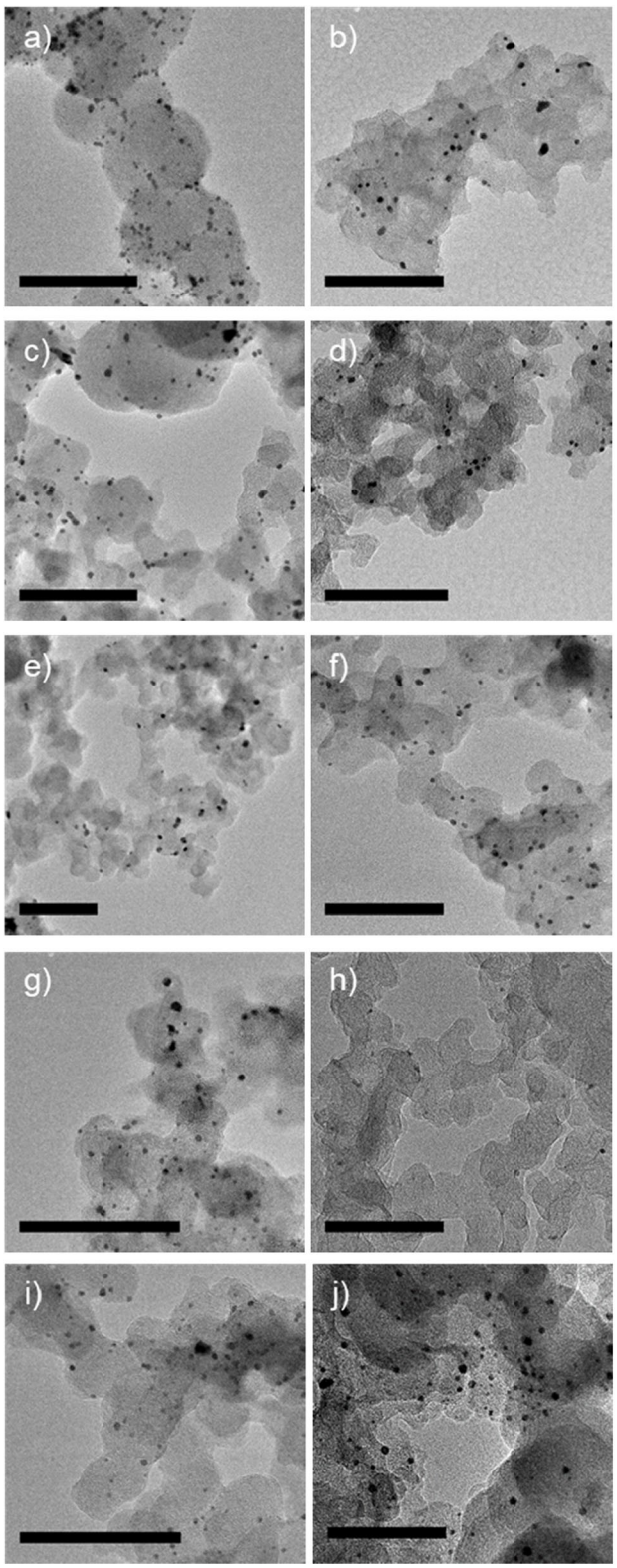


**Figure 3.** TEM images of carbon-supported Au/Cu NPs which were synthesized in [BMPyrr][FAP], [MMPyrr][FAP], and [BMPyrr][$NTf_2$] using different ratios of the Au and Cu precursors: a) $Au_3Cu$ in [BMPyrr][FAP] ($Au_3Cu$–A1 NPs 1), b) $Au_3Cu$ in [MMPyrr][FAP] ($Au_3Cu$–A1 NPs 4), c) $Au_3Cu$ in [BMPyrr][$NTf_2$] ($Au_3Cu$–A1 NPs 7), d) AuCu in [BMPyrr][FAP] (AuCu–A1 NPs 2), e) AuCu in [MMPyrr][FAP] (AuCu–A1 NPs 5), f) AuCu in [BMPyrr][$NTf_2$] (AuCu–A1 NPs 8), g) $AuCu_3$ in [BMPyrr][FAP] ($AuCu_3$–A1 NPs 3), h) $AuCu_3$ in [MMPyrr][FAP] ($AuCu_3$–A1 NPs 6), i) $AuCu_3$ in [BMPyrr][$NTf_2$] ($AuCu_3$–A1 NPs 9), j) Au NPs in [BMPyrr][$NTf_2$] (Au NPs 10). (Scale bar: 100 nm).

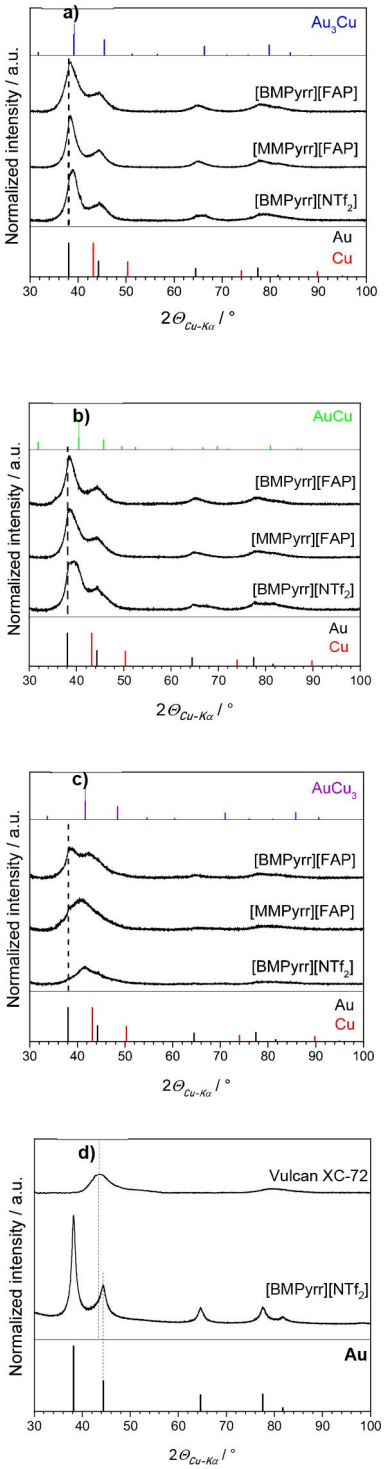


**Figure 4.** Diffraction patterns of the carbon-supported Au/Cu NPs with molar Au/Cu precursor ratio of a) 3:1 ($Au_3Cu$–A1 NPs 1, 4 and 7), b) 1:1 (AuCu–A1 NPs 2, 5 and 8) and c) 1:3 ($AuCu_3$–A1 NPs 3, 6 and 9) which were obtained in [BMPyrr][FAP], [MMPyrr][FAP], and [BMPyrr][$NTf_2$]. d) XRD pattern of monometallic Au NPs 10 obtained in [BMPyrr][$NTf_2$] and the carbon support Vulcan XC-72. (References: Au (ICDD 03-065-2870, black), Cu (ICDD 00-004-0836, red), $Au_3Cu$ (ICDD 98-005-6266, blue), AuCu (ICDD 00-025-1220, green), $AuCu_3$ (ICDD 00-035-1357, purple)).

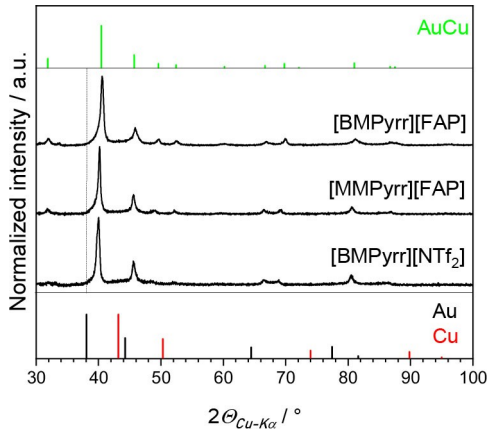


**Figure 5.** Diffraction patterns of the carbon-supported AuCu NPs (Au/Cu precursor ratio 1:1) synthesized in [BMPyrr][FAP] (AuCu–$L1_0$ NPs 11), [MMPyrr][FAP] (AuCu–$L1_0$ NPs 12), and [BMPyrr][$NTf_2$] (AuCu–$L1_0$ NPs 13) after annealing at 400 °C. (References: Au (ICDD 03-065-2870, black), AuCu (ICDD 00-025-1220, green), Cu (ICDD 00-004-0836, red).

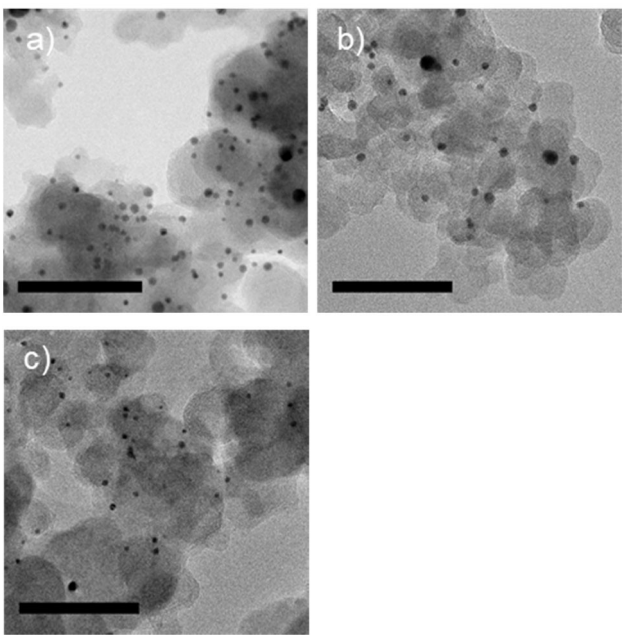


**Figure 6.** TEM images of carbon-supported AuCu NPs (molar Au/Cu precursor ratio 1:1) which were synthesized in a) [BMPyrr][FAP] (AuCu–$L1_0$ NPs 11), b) [MMPyrr][FAP] (AuCu–$L1_0$ NPs 12), and c) [BMPyrr][$NTf_2$] (AuCu–$L1_0$ NPs 13) and successively annealed at 400 °C for 1 h (Scale bar: 100 nm).

increased slightly to 5.3 nm (AuCu–$L1_0$ NPs 13; Table 2, entry 13) and 7.2 nm (AuCu–$L1_0$ NPs 12; Table 2, entry 12). In all samples, the crystallite size estimated by the Scherrer equation was larger than the average NP size measured by TEM. It should be noted that the Scherrer formula does not consider particle size distributions; if both a few large and small NPs are present in the sample. The diffraction profile represents a convolution of narrow and broad reflections, whereby the narrow reflections of larger NPs dominate the profile.

**Table 2.** Summary of mean particle sizes (based on TEM images) and crystallite sizes (calculated using the Scherrer equation) of supported, annealed AuCu NPs.

| NPs | Catalyst | IL | Average NP size[a] (nm) | Crystallite size[b] (nm) |
|---|---|---|---|---|
| **11** | AuCu–$L1_0$ | [BMPyrr][FAP] | 5.9 ± 1.7 | 11.0 |
| **12** | AuCu–$L1_0$ | [MMPyrr][FAP] | 7.2 ± 2.2 | 15.5 |
| **13** | AuCu–$L1_0$ | [BMPyrr][$NTf_2$] | 5.3 ± 1.6 | 12.4 |

[a] Particle sizes were determined based on TEM images (measuring at least the size of 300 NPs). [b] Crystallite sizes calculated by the Scherrer equation using the FWHM of the 101 reflection.

The results of the XPS characterization of the carbon-supported Au/Cu NPs with a Au/Cu ratio of 1:1 are presented in Table 3 and Figure 7. The binding energy (BE) values of the Au $4f_{7/2}$ and Cu $2p_{3/2}$ elemental lines of both non-annealed and annealed samples are in a range of (84.3–84.4) eV and (932.4–932.6) eV, which is consistent with the zero valent oxidation state, respectively.[6f,9g,30,31] In all samples, the Au $4f_{7/2}$ elemental lines are shifted to slightly higher BE values compared to pure Au bulk, similar to what is observed for Au/Cu alloys.[30a] The narrowing of elemental line widths after annealing could be the result of NP growth and increase of order. Sometimes, it is not possible to distinguish between Cu(0), Cu(I), and Cu(II) based on the Cu $2p_{3/2}$ BE alone. The presence of shake-up satellites at the Cu 2p elemental lines is characteristic for Cu(II) compounds, but shake-up satellites are not observed in this case (Figure S9a and b). Besides Cu–Au interaction, the presence of Cu, $Cu_2O$, and $Cu_2S$ species is possible, based on the detected elements, absence of intense shake-up satellites, and similar BE of Cu $2p_{3/2}$ elemental lines reported, i.e. 932.62 eV, (932.0–932.8) eV, and (932.0–932.9) eV, respectively.[32] However, copper sulfides are excluded since S $2p_{3/2}$ elemental lines of black carbon and carbon-supported NPs show a BE of 163.9 eV, in-line with elemental sulfur or sulfur in an organic matrix, but BEs of Cu $2p_{3/2}$ of copper sulfides are reported within the range of (161.3–162.7) eV (Figure S9c and d).[32] Weak shake-up satellites are observed for Cu 2p ($Cu_2O$) besides the plasmon-loss lines,[33] but satellites are not detected for the carbon-supported NPs. However, it should be noted that the main lines reveal a low

**Table 3.** Binding energy (BE), full width at half maximum (FWHM) of the carbon-supported AuCu NPs after annealing at 400 °C as determined by XPS analysis.

| Entry | BE Au $4f_{7/2}$ [FWHM] [± 0.15 eV] | | BE $Cu2p_{3/2}$ [FWHM] [± 0.15 eV] | |
|---|---|---|---|---|
| Bulk References[30] | Au (Metal) | AuCu (Alloy) | Cu (Metal) | AuCu (Alloy) |
| | 83.96 | 84.3 | 932.62 | 932.4 |
| AuCu–A1 NPs 2 | 84.3 (0.90) | | 932.4 (1.13) | |
| AuCu–$L1_0$ NPs 11 | 84.4 (0.84) | | 932.6 (1.11) | |
| AuCu–$A_1$ NPs 5 | 84.3 (0.90) | | 932.5 (1.25) | |
| AuCu–$L1_0$ NPs 12 | 84.4 (0.87) | | 932.6 (1.14) | |
| AuCu–$A_1$ NPs 8 | 84.3 (0.87) | | 932.5 (1.32) | |
| AuCu–$L1_0$ NPs 13 | 84.4 (0.84) | | 932.6 (1.25) | |

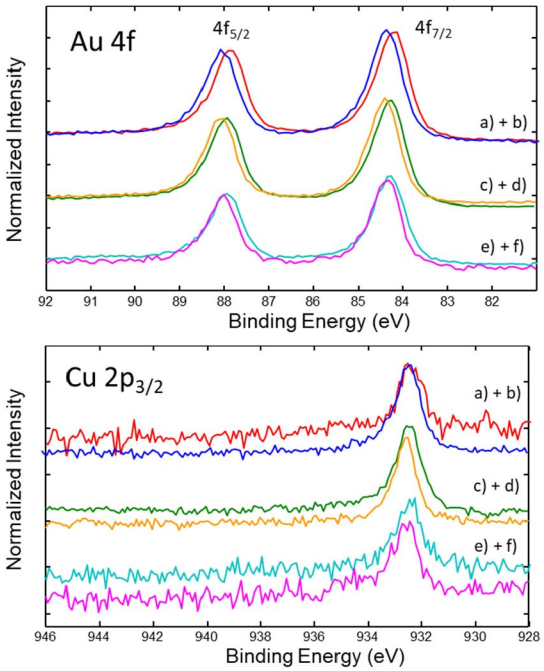


**Figure 7.** XPS spectra of the carbon-supported AuCu NPs synthesized in [BMPyrr][FAP], [MMPyrr][FAP], and [BMPyrr][$NTf_2$] (molar Au/Cu precursor ratio 1:1)before and after annealing at 400 °C: a) AuCu-A1 NPs 2 (red), b) AuCu-$L1_0$ NPs 11 (blue), c) AuCu-A1 NPs 5 (green), d) AuCu-$L1_0$ NPs 12 (orange), e) AuCu-A1 NPs 8 (turquoise), and f) AuCu-$L1_0$ NPs 13 (magenta).

intensity and spectral noise. BE references of O 1s ($Cu_2O$) are within (530.2–530.7) eV, but, due to low atomic concentration of Cu compared to O, the corresponding portion of Cu–O bonding at the O 1s spectrum cannot be deciphered. For carbon-supported NPs, XPS cannot discriminate between Cu–Au interaction, Cu, and $Cu_2O$, but $Cu_2O$ was also not detected by XRD analysis. For most samples, XPS shows similar atomic concentrations for Au and Cu of the NPs within experimental accuracy (Table S1 in the SI). An overview on the XPS spectra is also displayed in Figure S9e in the SI. For the non-annealed AuCu–A1 catalysts (carbon-supported AuCu–A1 NPs 2, 5 and 8), XPS spectra also indicate some IL residues on the catalyst surface by detection of F signals of the $[FAP]^-$ and – to a lesser extend – the $[NTf_2]^-$ anions. For both samples, these F signals decrease after the annealing step: While some F containing species are still observed, e.g., for carbon-supported AuCu–$L1_0$ NPs 11, no F signal is detected for carbon-supported AuCu–L10 NPs 13 (Table S1 in the SI). However, it should be noted that the error related to atomic composition by XPS analysis is high.

In the present work, the aerobic oxidation of 5-hydroxymethyl-2-furfural (HMF) (Figure 8) was chosen as a model reaction to study the catalytic performance of the carbon-supported Au/Cu NP catalysts and the effect of Cu addition.

For the catalytic tests, the carbon-supported Au/Cu NP catalysts were suspended in aqueous HMF solution and the selective oxidation was carried out in air (10 bar, 100 °C) with

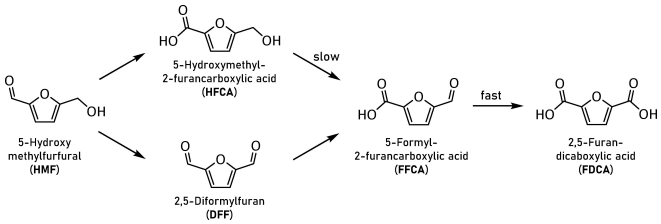


**Figure 8.** Reaction pathways for the oxidation of HMF.

excess of NaOH (see Experimental section). All carbon-supported, NP-based catalysts (Tables 1, 2) were tested in the HMF oxidation reaction. Table 4 summarizes the yield of HFCA and FDCA as determined by HPLC analysis. Au NPs 10 synthesized in [BMPyrr][$NTf_2$] were used as a reference. In the presence of our bimetallic Au/Cu NP catalysts, the main product was FDCA (Figure 8) while some HFCA was also detected in particular for catalysts with high Cu content (Au/Cu ratio 1:3). The reaction without catalyst and in the presence of the carbon support only led to a negligible amount of HFCA and FDCA (Table 4, entry 14 and 13). Alcohol oxidation in HFCA was suggested to be the rate-limiting step while the FFCA intermediate (if formed) was quickly transformed to FFCA.[29] This is in good agreement with our results where no FFCA intermediate was detected. Monometallic Au NPs 10 yielded 65% FDCA as the main product (entry 15). In contrast, depending on the catalyst composition of the bimetallic alloys, the FDCA yield differed significantly.

As a general trend, the Au-rich catalysts $Au_3Cu$–A1 NPs 1 and NPs 7 (entries 1, 7) and AuCu–A1 NPs 2, NPs 5 and NPs 8 (Table 4, entries 2, 5, 8) showed higher FDCA yields compared to the monometallic Au NPs 10. In this context, the FDCA yield decreased with increasing Cu content indicating a lower activity for HMF oxidation as compared to the Au-rich catalysts

**Table 4.** Summary of the catalytic performance of the carbon-supported Au/Cu NP catalysts (reaction conditions: air (10 bar), 100 °C, NaOH/HMF molar ratio 4, 300 min, molar HMF/metal ratio 100; HMF conversion (*X*), turn over numbers (TONs) refer to the FDCA/HFCA product formed).

| N° | Catalyst | *X* HMF [%] | Yield (%) | | TONs[a] | |
|---|---|---|---|---|---|---|
| | | | HFCA | FDCA | HFCA | FDCA |
| **1** | $Au_3Cu$–A1 NPs 1 | 100 | 0 | 91 ± 1 | 0 | 263 |
| **2** | AuCu–A1 NPs 2 | 100 | 0 | 78 ± 4 | 0 | 259 |
| **3** | $AuCu_3$–A1 NPs 3 | 100 | 4 ± 1 | 21 ± 10 | 13 | 71 |
| **4** | $Au_3Cu$–A1 NPs 4 | 100 | 4 ± 1 | 46 ± 6 | 16 | 183 |
| **5** | AuCu–A1 NPs 5 | 100 | 0 | 78 ± 8 | 0 | 290 |
| **6** | $AuCu_3$–A1 NPs 6 | 100 | 16 ± 4 | 10 ± 6 | 66 | 41 |
| **7** | $Au_3Cu$–A1 NPs 7 | 100 | 0 | 90 ± 1 | 0 | 293 |
| **8** | AuCu–A1 NPs 8 | 100 | 0 | 66 ± 0 | 0 | 266 |
| **9** | $AuCu_3$–A1 NPs 9 | 100 | 13 ± 2 | 25 ± 5 | 37 | 72 |
| **10** | AuCu–$L1_0$ NPs 11 | 100 | 0 | 60 ± 10 | 0 | 307 |
| **11** | AuCu–$L1_0$ NPs 12 | 100 | 5 ± 3 | 1 ± 0 | 30 | 6 |
| **12** | AuCu–$L1_0$ NPs 13 | 100 | 7 ± 3 | 7 ± 3 | 31 | 31 |
| **13** | carbon | 100 | 1 ± 2 | 5 ± 2 | - | – |
| **14** | no catalyst | 100 | 1 | 1 | - | – |
| **15** | Au NPs 10 | 100 | 2 ± 2 | 65 ± 8 | 9 | 282 |

[a] For calculation of TONs see SI. The fraction of atoms on the NP surface were estimated using the closest magic atom numbers of full shell NPs with ideal cuboctahedral or icosahedral shapes.

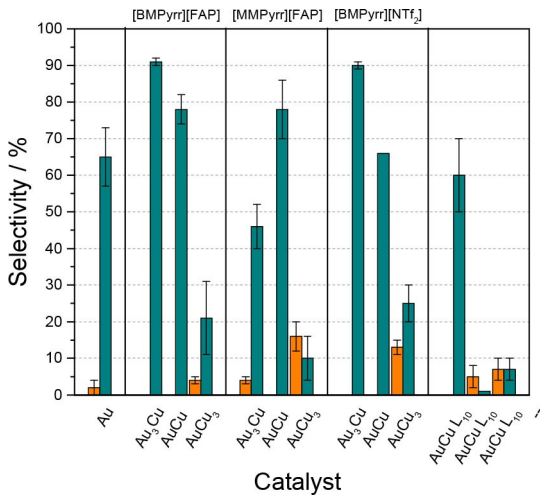


**Figure 9.** FDCA and HFCA selectivities of the carbon-supported Au/Cu NP catalysts (FDCA: turquoise; HFCA: orange).

$Au_3Cu$–A1 NPs 1 and NPs 7 (entries 1, 7) and AuCu–A1 NPs 2, NPs 5 and NPs 8 (entries 2, 5, 8), respectively. A similar trend was observed for the turn over numbers (TONs) where TONs decreased with increasing Cu content from 263 to 259 for $Au_3Cu$–A1 NPs 1 and AuCu–A1 NPs 2 and from 293 to 266 for $Au_3Cu$–A1 NPs 7 and AuCu–A1 NPs 8, respectively. For $Au_3Cu$–A1 NPs 4 (Table 4, entry 4), the FDCA yield was lower than for AuCu–A1 NPs 5 (entry 5) which could be the result of the larger particle size and/or agglomerate formation (Figure S2 in the SI). $AuCu_3$–A1 NPs 6 (Table 4, entry 6) revealed the lowest FDCA yield of all $AuCu_3$ catalysts. Overall, Cu alloying enhanced the FDCA selectivity as compared to monometallic Au NP reference, indicating a synergistic effect in the bimetallic nanocatalysts. The beneficial effect of the Cu dopant was most prominent for catalysts with a molar Au/Cu ratio of 3:1 and decreased with further incorporation of Cu (molar ratio Au/Cu 1:1 and 1:3). It should be noted that monometallic Cu is not a selective catalyst for HMF oxidation and no FDCA is formed.[31] In good agreement with our results, the active phase composition in $TiO_2$-supported Au/Cu catalysts was previously demonstrated to influence the catalytic performance in HMF oxidation where the selectivity to the desired FDCA significantly increased for Au/Cu of 3:1 and 1:1 with respect to the monometallic systems and afterwards decreased as the Cu content further increased in the catalyst formulation.[9d] Entries 10–12 (Table 4) show the catalytic performance of the Au/Cu catalysts with intermetallic AuCu $L1_0$ structure formed after annealing at 400 °C. The FDCA yield was lower compared to the non-annealed Au/Cu-based counterparts (entry 10) while the amount of FDCA formed was negligible for AuCu–$L1_0$ NPs 12 (entry 11) and AuCu–$L1_0$ NPs 13 (entry 12). However, if the increased size of the AuCu–$L1_0$ NPs 10 (i.e. 5.9 (±1.7) nm (TEM) and 2.8 nm (XRD)) compared to the AuCu–A1 NPs 2 (i.e. 3.9 (±0.9) nm (TEM) and 11.0 nm (XRD)) was considered, an increase in TON was observed from 259 to 307 for AuCu–A1 NPs 2 and AuCu–$L1_0$ NPs 10, respectively. This could indicate a beneficial effect of the intermetallic $L1_0$ structure in this case. In general, beneficial effects of Au/Cu catalysts in HMF oxidation have been ascribed to Au site isolation effects caused by alloying with Cu.[31] The authors also particularly emphasized the importance of the bimetallic catalyst synthesis procedure and the essential synergistic interaction between Au and Cu components in order to achieve the desired Cu promotional effect in Au.[27] It should be further noted that residues of IL anions or cations or their decomposition during the annealing step may further influence the catalytic properties of entries 10, 11, and 12.

For all catalysts and even in the absence of catalyst, the conversion of HMF was quantitative (*X*(HMF) 100%) due to its instability in alkaline solution leading to several by-products.[34] However, addition of NaOH enhances HMF oxidation suggesting a crucial role of soluble base to increase FDCA yield. Mechanistic studies by $^{18}O$ labeling experiments suggested that the oxidation of HMF proceeds *via* formation of geminal diol through the reaction of the aldehyde with solvent.[35] HFCA does not decompose/polymerize under these reaction conditions and hence, a high HMF oxidation activity (step 1; aldehyde oxidation) is also highly desirable to increase the yield of the desired FDCA product.

## Conclusion

In conclusion, we show the synthesis of small, bimetallic Au/Cu NPs with a 3:1, 1:1 and 1:3 composition employing different ILs without the use of additional capping agents. The NPs were successively immobilized on a carbon support, and the IL could be recycled for subsequent NP synthesis procedures. The as-prepared Au/Cu NPs were homogeneously distributed over the carbon support and initially revealed a solid solution-type, fcc structure and sizes in the range of 3.3–5.2 nm and 2.2–6.5 nm according to TEM and XRD analysis, respectively. Annealing of the carbon-supported Au/Cu NPs at 400 °C led to the formation of AuCu NPs with the ordered, intermetallic $L1_0$ structure and to an increase in NP size to 5.3–7.2 nm and 11.0–12.4 nm based on TEM and XRD analysis, respectively. The influence of Cu addition in the Au/Cu NPs was demonstrated in the aerobic HMF oxidation in alkaline conditions with yields of the desired FDCA of up to 91%. FDCA selectivity significantly increased for Au/Cu NP compositions of 3:1 and 1:1 with respect to the monometallic Au NPs and afterwards decreased as the Cu content further increased to Au/Cu 1:3. Synergistic interaction between Au and Cu components seemed to be essential to achieve the desired Cu promotional effect in Au for HMF oxidation. Considering the increase in NP size after annealing at 400 °C for intermetallic AuCu $L1_0$ NPs synthesized in [BMPyrr][FAP], the TONs even further increased with respect to the Au/Cu NPs (Au/Cu ratio 1:1) with solid solution-type structure. It should be noted that especially in case of AuCu $L1_0$ NPs, the bimetallic catalyst synthesis procedure was important with respect to catalytic performance. Further enhancement of catalytic properties may be expected in future work by further optimizing the reaction conditions.

## Experimental Section

***Materials***: All chemicals were of analytical grade and used without further purification if not stated differently. HMF, FDCA, HFCA, NaOH, $HAuCl_4$*3 $H_2O$, $CuCl_2$*2 $H_2O$, [BMPyrr][FAP], [MMPyrr][FAP], [BMPyrr][BTA], $Li[BEt_3H]_{THF}$ (1 M in THF) were purchased from Merck/Sigma Aldrich. Acetonitrile (MeCN) and tetrahydrofuran (THF) were received from Sigma Aldrich. 5-formyl-2-furoic acid and DFF were obtained from TCI Chemicals; Carbon Black Vulcan-XC 72 was from Degussa. Synthetic air was obtained from Air Liquide. Prior to use, $HAuCl_4$*3 $H_2O$, $CuCl_2$*2 $H_2O$ and the ILs were dried in vacuum ($1*10^{-2}$ mbar) at 50 °C–80 °C for several hours. All steps of NP synthesis and catalyst preparation were carried out under argon atmosphere.

**Synthesis of bimetallic Au/Cu NPs in ILs**: Depending on the composition, the appropriate amounts of $HAuCl_4$ and $CuCl_2$ (total 0.25 mmol) were dispersed in the IL (4 mL) by stirring for several hours. To this mixture, 1.3 mL $Li[BEt_3H]$ (1.3 mmol in THF) was added with a syringe and the reaction mixture was stirred at room temperature for 5 hours. The as-received NP sols were further used for catalyst preparation.

**Preparation of supported Au/Cu NP catalysts**: Cabon-Black Vulcan-XC 72 was used as a support material to immobilize the NPs from the NP sol in the IL. For catalysts with a total metal loading of 10 wt%, an appropriate amount of the carbon support was suspended in MeCN/THF (1:1, 20 mL) by magnetic stirring and ultrasonication for several hours. Then, the NP sol in the IL was added dropwise to the suspended carbon support material while stirring. The suspension was stirred for another 30 min and dispersed by ultrasonication for several hours. The catalyst powder was collected by centrifugation (1050 rcf, 5 min). The supernatant was clear and collected to recycle the IL. The catalyst powder was subsequently washed with MeCN, MeCN/THF and THF. Eventually, the supported Au/Cu catalysts were dried in vacuum at room temperature overnight.

**Annealing of supported NPs**: The Au/Cu NPs were annealed by transferring the catalyst powder to a quartz ampule, evacuating for several hours, and heating to 400 °C in the oven for 1 hour.

**Characterization**: X-Ray diffraction (XRD) analysis of the powder catalysts was performed on a PANalytical X'Pert Pro instrument using a Bragg-Brentano geometry with Cu–$K_\alpha$ radiation (1.54060 Å) and a Ni filter. The diffractograms were recorded from 20° to 100° ($2\theta$) over a period lasting two times 2 h at room temperature. The reflections were compared to reference data reported in the Joint Committee of Powder Diffraction Standards (JCPD) database (References: Au (ICDD 03-065-2870), Cu (ICDD 00-004-0836), $Au_3Cu$ (ICDD 98-005-6266), AuCu (ICDD 00-025-1220), $AuCu_3$ (ICDD 00-035-1357, LiF (ICDD 01-070-1934). The metal loading of the catalysts and the concentrations of metals in the reaction solutions were determined by ICP-OES (Agilent 720/725-ES instrument). For ICP-OES analysis, the powder catalysts were digested in a mixture of HCl, $HNO_3$ and $H_2O_2$. For electron microscopy studies, the catalysts were mounted on carbon-coated Ni grids by dispersing the catalyst powders in THF and then applying a droplet onto the grid which was air-dried. The samples were examined using an FEI Tecnai F20 ST TEM (operating voltage 200 kV), which was equipped with a field emission gun and EDAX EDS X-ray spectrometer and by SEM on a Zeiss GeminiSEM500, equipped with a Schottky-type thermal field emission cathode. XPS measurements were performed by an XPS system PHI 5000 VersaProbe II (ULVAC-PHI Inc.) equipped with a scanning microprobe X-ray source [monochromatic Al–$K_\alpha$ (1486.7 eV) X-rays]. Survey scans were recorded with an X-ray source power of 33 W and pass energy of 117.4 eV. Narrow scans of the elemental lines were recorded at 23.5 eV pass energy, which yields an energy resolution of 0.69 eV FWHM at the Ag $3d_{5/2}$ elemental line of pure silver, 0.80 eV FWHM at the Au $4f_{7/2}$ elemental line of pure gold, and 0.90 eV FWHM at the Cu $2p_{3/2}$ elemental line of pure copper. Calibration of the binding energy scale of the spectrometer was performed using well-established binding energies of elemental lines of pure metals (monochromatic Al–Kα: Cu $2p_{3/2}$ at 932.62 eV, Au $4f_{7/2}$ at 83.96 eV).[30b] Binding energies of elemental lines of the samples were charge referenced to C 1s (carbon black) 284.5 eV. To determine the BE of the Cu $2p_{3/2}$ element lines, the XPS spectra were smoothed using the Savitzky-Golay convolution algorithm 15-points and the maxima were determined (Figure S9a and b in the SI). The FWHM were also determined using the smoothed spectra. If the raw data are treated by curve fitting, it is difficult to set the endpoints so that the background function, e.g., Shirley-background, is set properly because of the noise. It should be further noted that, due to noise, shoulders at some Cu $2p_{3/2}$ element lines are not significant. Samples were prepared on pieces of silicon wafer, mounted on the sample holder inside an anoxic glove box and moved into the XPS by means of a vacuum transfer vessel. Data analysis was performed using ULVAC-PHI MultiPak program (version 9.9).

**Catalytic tests**: The catalytic performance of the supported catalysts in the oxidation of HMF was carried out in a stainless steel batch reactor with Teflon liner (52 mL, max. 200 bar, 350 °C) while magnetic stirring. In a typical catalytic test, 5 mL aqueous HMF solution (0.2 M), 1.6 mL NaOH solution (2.5 M) and 3.4 mL water were added to the reactor. After addition of the catalyst (0.01 mmol total metal content (Au and Cu) per experiment, i.e. 15.9 mg ($Au_3Cu$–A1 NPs 1), 15.0 mg (AuCu–A1 NPs 2), 11.7 mg ($AuCu_3$–A1 NPs 3), 15.3 mg ($Au_3Cu$–A1 NPs 4), 15.3 mg (AuCu–A1 NPs 5), 11.3 mg ($AuCu_3$–A1 NPs 6), 14.7 mg ($Au_3Cu$–A1 NPs 7), 15.3 mg (AuCu–A1 NPs 8), 11.5 mg ($AuCu_3$–A1 NPs 9), 28.1 mg (Au NPs 10), 15.0 mg (AuCu–$L1_0$ NPs 11), 15.3 mg (AuCu–$L1_0$ NPs 12), 11.5 mg (AuCu–$L1_0$ NPs 13)) and purging three times with synthetic air, the reactor was pressurized to 10 bar. The reactor was heated to 100 °C with a heating plate and a heating sleeve. The start of the reaction ($t_0$) was set when the solution first reached the set temperature. After the reaction, the autoclave was cooled to room temperature in an ice bath, depressurized and the catalysts were separated by centrifugation. Conversion, product yield and selectivity were calculated based on HPLC analysis (Hitachi Primaide, Bio-Rad Aminex HPX-87H column, solvent 5 mM $H_2SO_4$, temperature 50 °C, 50 bar) of the reactant and product solutions. Every catalytic test was carried out at least twice. The measurement uncertainty of the catalytic tests is related to sample pipetting, inhomogeneity or electrostatic charging of catalyst etc. and was roughly estimated by dividing the difference between the respective extreme values by the number of experiments. Conversion ($X$(HMF) [%]), selectivity ($S$(FDCA) [%]) and yield ($Y$(FDCA) [%]) were calculated from peak areas, after calibration using commercial reference samples (regression coefficients: 0.9994 (HMF), 0.9993 (HFCA), 0.9915 (FDCA)), according to the following equations:

$$X\ (HMF) = \frac{n_{HMF,0} - n_{HMF,t}}{n_{HMF,0}} \cdot 100 \quad (1)$$

with $n_{FDCA,t}$ moles FDCA at time $t$, $n_{HMF,0}$ and $n_{HMF,t}$ moles HMF at reaction start and after time $t$.

HFCA selectivity and yield was calculated with $n_{HFCA}$ and $S_{HFCA}$ according to [Eq. (2) and (3)].

$$S\ (FDCA) = \frac{n_{FDCA,t}}{n_{HMF,\,0} - n_{HMF,\,t}} \cdot 100 \quad (2)$$

$$Y\ (FDCA) = X_{HMF} \cdot S_{FDCA} \cdot 10^{-2} \quad (3)$$

## Acknowledgements

We would like to thank A. Lauterbach and S. Habicht for ICP-AES and HPLC measurements, respectively. Financial support provided by the German Science Foundation (DFG) within the Priority Program (SPP1708) "Material Synthesis near Room Temperature" (projects BE 2243/3-1 and BE 2243/3-2) is gratefully acknowledged. Open access funding enabled and organized by Projekt DEAL.

## Conflict of Interest

The authors declare no conflict of interest.

**Keywords:** bimetallic Au/Cu nanoparticles · ionic liquids · oxidation · hydroxymethyl furfural · intermetallic nanoparticles

[1] G. Guisbiers, S. Mejia-Rosales, S. Khanal, F. Ruiz-Zepeda, R. L. Whetten, M. José-Yacaman, *Nano Lett.* **2014**, *14*, 6718–6726.
[2] C. L. Bracey, P. R. Ellis, G. J. Hutchings, *Chem. Soc. Rev.* **2009**, *38*, 2231–2243.
[3] a) S. Furukawa, T. Komatsu, *ACS Catal.* **2017**, *7*, 735–765; b) Y. Yan, J. S. Du, K. D. Gilroy, D. Yang, Y. Xia, H. Zhang, *Adv. Mater.* **2017**, *29*, 1605997-n/a; c) A. K. Singh, Q. Xu, *ChemCatChem* **2013**, *5*, 652–676.
[4] a) M. Sankar, N. Dimitratos, P. J. Miedziak, P. P. Wells, C. J. Kiely, G. J. Hutchings, *Chem. Soc. Rev.* **2012**, *41*, 8099–8139; b) D. I. Sharapa, D. E. Doronkin, F. Studt, J.-D. Grunwaldt, S. Behrens, *Adv. Mater.* **2019**, *31*, 1807381; c) C. Dietrich, M. Hähsler, W. Wang, C. Kübel, S. Behrens, *ChemNanoMat* **2020**, *6*, 1854–1862; d) M. Gentzen, D. E. Doronkin, T. L. Sheppard, A. Zimina, H. Li, J. Jelic, F. Studt, J.-D. Grunwaldt, J. Sauer, S. Behrens, *Angew. Chem. Int. Ed.* **2019**, *58*, 15655–15659; *Angew. Chem.* **2019**, *131*, 15802–15806; e) S. K. Singh, M. Yadav, S. Behrens, P. W. Roesky, *Dalton Trans.* **2013**, *42*, 10404–10408.
[5] a) V. Mazumder, Y. Lee, S. Sun, *Adv. Funct. Mater.* **2010**, *20*, 1224–1231; bÇ. C. Bakır, N. Şahin, R. Polat, Z. Dursun, *J. Electroanal. Chem.* **2011**, *662*, 275–280.
[6] a) C. Della Pina, E. Falletta, L. Prati, M. Rossi, *Chem. Soc. Rev.* **2008**, *37*, 2077–2095; b) H. Xia, S. Xu, H. Hu, J. An, C. Li, *RSC Adv.* **2018**, *8*, 30875–30886; c) C. L. Bracey, A. F. Carley, J. K. Edwards, P. R. Ellis, G. J. Hutchings, *Catalysis Science, Technology* **2011**, *1*, 76–85; d) J. C. Bauer, G. M. Veith, L. F. Allard, Y. Oyola, S. H. Overbury, S. Dai, *ACS Catal.* **2012**, *2*, 2537–2546; e) Y. Bing, H. Liu, L. Zhang, D. Ghosh, J. Zhang, *Chem. Soc. Rev.* **2010**, *39*, 2184–2202; f) S. Albonetti, A. Lolli, V. Morandi, A. Migliori, C. Lucarelli, F. Cavani, *Appl. Catal. B* **2015**, *163*, 520–530.
[7] a) J. Li, S. Sun, *Acc. Chem. Res.* **2019**, *52*, 2015–2025; b) J. C. Bauer, D. Mullins, M. Li, Z. Wu, E. A. Payzant, S. H. Overbury, S. Dai, *Phys. Chem. Chem. Phys.* **2011**, *13*, 2571–2581; c) J. Yin, S. Shan, L. Yang, D. Mott, O. Malis, V. Petkov, F. Cai, M. Shan Ng, J. Luo, B. H. Chen, M. Engelhard, C.-J. Zhong, *Chem. Mater.* **2012**, *24*, 4662–4674.
[8] a) P. P. Fedorov, S. N. Volkov, *Russ. J. Inorg. Chem.* **2016**, *61*, 772–775; b) T. Tadaki, A. Koreeda, Y. Nakata, T. Kinoshita, *Surf. Rev. Lett.* **1996**, *3*, 65–69; c) T. Tadaki, T. Kinoshita, Y. Nakata, T. Ohkubo, Y. Hirotsu, *Z. Phys. D* **1997**, *40*, 493–495.
[9] a) U. Pal, J. F. Sanchez Ramirez, H. B. Liu, A. Medina, J. A. Ascencio, *Appl. Phys. A* **2004**, *79*, 79–84; b) A. K. Sra, T. D. Ewers, R. E. Schaak, *Chem. Mater.* **2005**, *17*, 758–766; c) T. Pasini, M. Piccinini, M. Blosi, R. Bonelli, S. Albonetti, N. Dimitratos, J. A. Lopez-Sanchez, M. Sankar, Q. He, C. J. Kiely, G. J. Hutchings, F. Cavani, *Green Chem.* **2011**, *13*, 2091–2099; d) S. Albonetti, T. Pasini, A. Lolli, M. Blosi, M. Piccinini, N. Dimitratos, J. A. Lopez-Sanchez, D. J. Morgan, A. F. Carley, G. J. Hutchings, F. Cavani, *Catal. Today* **2012**, *195*, 120–126; e) C. M. Andolina, A. C. Dewar, A. M. Smith, L. E. Marbella, M. J. Hartmann, J. E. Millstone, *J. Am. Chem. Soc.* **2013**, *135*, 5266–5269; f) S. K. Sinha, C. Srivastava, S. Sampath, K. Chattopadhyay, *RSC Adv.* **2015**, *5*, 4389–4395; g) G. Wang, L. Xiao, B. Huang, Z. Ren, X. Tang, L. Zhuang, J. Lu, *J. Mater. Chem.* **2012**, *22*, 15769–15774.
[10] a) Ş. Neaţu, J. A. Maciá-Agulló, P. Concepción, H. Garcia, *J. Am. Chem. Soc.* **2014**, *136*, 15969–15976; b) L. Rout, A. Kumar, R. S. Dhaka, G. N. Reddy, S. Giri, P. Dash, *Appl. Catal. A* **2017**, *538*, 107–122.
[11] D. M. Hofmann, D. H. Fairbrother, R. J. Hamers, C. J. Murphy, *ACS Applied Nano Materials* **2019**, *2*, 3989–3998.
[12] W. Chen, R. Yu, L. Li, A. Wang, Q. Peng, Y. Li, *Angew. Chem. Int. Ed.* **2010**, *49*, 2917–2921; *Angew. Chem.* **2010**, *122*, 2979–2983.
[13] Y. Liu, A. R. H. Walker, *Angew. Chem. Int. Ed.* **2010**, *49*, 6781–6785; *Angew. Chem.* **2010**, *122*, 6933–6937.
[14] R. He, Y.-C. Wang, X. Wang, Z. Wang, G. Liu, W. Zhou, L. Wen, Q. Li, X. Wang, X. Chen, J. Zeng, J. G. Hou, *Nat. Commun.* **2014**, *5*, 4327.
[15] Y. Xia, Y. Xiong, B. Lim, S. E. Skrabalak, *Angew. Chem. Int. Ed.* **2009**, *48*, 60–103; *Angew. Chem.* **2009**, *121*, 62–108.
[16] a) A. Quintanilla, V. C. L. Butselaar-Orthlieb, C. Kwakernaak, W. G. Sloof, M. T. Kreutzer, F. Kapteijn, *J. Catal.* **2010**, *271*, 104–114; b) D. I. Sharapa, D. E. Doronkin, F. Studt, J.-D. Grunwaldt, S. Behrens, *Adv. Mater.* **2019**, *31*, 1807381; c) P. Liu, R. Qin, G. Fu, N. Zheng, *J. Am. Chem. Soc.* **2017**, *139*, 2122–2131.
[17] a) C. Janiak, *Z. Naturforsch. B* **2013**, *68*, 1059; b) M. Vranes, S. Dozic, V. Djeric, S. Gadzuric, *J. Chem. Eng. Data* **2012**, *57*, 1072–1077; c) J. Salgado, J. J. Parajó, J. Fernández, M. Villanueva, *J. Chem. Thermodyn.* **2014**, *74*, 51–57; d) C. J. Raquel Marcos Esteban, in *Nanocatalysis in Ionic Liquids* (Ed.: M. H. G. Prechtl), Wiley-VCH Verlag GmbH & Co. KGaA, **2016**, pp. 147–169.
[18] S. Essig, S. Behrens, *Chem. Ing. Tech.* **2015**, *87*, 1741–1747.
[19] D. König, K. Richter, A. Siegel, A.-V. Mudring, A. Ludwig, *Adv. Funct. Mater.* **2014**, *24*, 2049–2056.
[20] S. Suzuki, Y. Tomita, S. Kuwabata, T. Torimoto, *Dalton Trans.* **2015**, *44*, 4186–4194.
[21] a) K. Gupta, R. K. Rai, S. K. Singh, *ChemCatChem* **2018**, *10*, 2326–2349; b) K. Gupta, R. K. Rai, S. K. Singh, *Inorg. Chem. Front.* **2017**, *4*, 871–880; c) K. Gupta, R. K. Rai, A. D. Dwivedi, S. K. Singh, *ChemCatChem* **2017**, *9*, 2760–2767.
[22] a) D. Lei, K. Yu, M.-R. Li, Y. Wang, Q. Wang, T. Liu, P. Liu, L.-L. Lou, G. Wang, S. Liu, *ACS Catal.* **2017**, *7*, 421–432; b) Y. Liu, H.-Y. Ma, D. Lei, L.-L. Lou, S. Liu, W. Zhou, G.-C. Wang, K. Yu, *ACS Catal.* **2019**, *9*, 8306–8315.
[23] O. Schade, P. Dolcet, A. Nefedov, X. Huang, E. Saraçi, C. Wöll, J.-D. Grunwaldt, *Catalysts* **2020**, *10*, 342.
[24] S. E. Davis, L. R. Houk, E. C. Tamargo, A. K. Datye, R. J. Davis, *Catal. Today* **2011**, *160*, 55–60.
[25] O. Casanova, S. Iborra, A. Corma, *ChemSusChem* **2009**, *2*, 1138–1144.
[26] C. Megías-Sayago, K. Chakarova, A. Penkova, A. Lolli, S. Ivanova, S. Albonetti, F. Cavani, J. A. Odriozola, *ACS Catal.* **2018**, *8*, 11154–11164.
[27] T. Pasini, M. Piccinini, M. Blosi, R. Bonelli, S. Albonetti, N. Dimitratos, J. A. Lopez-Sanchez, M. Sankar, Q. He, C. J. Kiely, G. J. Hutchings, F. Cavani, *Green Chem.* **2011**, *13*, 2091–2099.
[28] a) S. Behrens, S. Essig, *J. Mater. Chem.* **2012**, *22*, 3811–3816; b) C. Dietrich, D. Schild, W. Wang, C. Kübel, S. Behrens, *Z. Anorg. Allg. Chem.* **2017**, *643*, 120–129.
[29] S. Essig, S. Behrens, *Chem. Ing. Tech.* **2015**, *87*, 1741–1747.
[30] a) M. Kuhn, T. K. Sham, *Phys. Rev. B* **1994**, *49*, 1647–1661; b) M. P. Seah, I. S. Gilmore, G. Beamson, *Surf. Interface Anal.* **1998**, *26*, 642–649.
[31] W. Zhan, J. Wang, H. Wang, J. Zhang, X. Liu, P. Zhang, M. Chi, Y. Guo, Y. Guo, G. Lu, S. Sun, S. Dai, H. Zhu, *J. Am. Chem. Soc.* **2017**, *139*, 8846–8854.
[32] NIST X-ray Photoelectron Spectroscopy Database, Version 4.1 (National Institute of Stand-ards and Technology, Gaithersburg, 2012); http://srdata.nist.gov/xps/.
[33] R. P. Vasquez, *Surf. Sci. Spectra* **1998**, 5 257–261.
[34] K. R. Vuyyuru, P. Strasser, *Catal. Today* **2012**, *195*, 144–154.
[35] S. E. Davis, B. N. Zope, R. J. Davis, *Green Chem.* **2012**, *14*, 143–147.

Manuscript received: June 15, 2021
Revised manuscript received: July 20, 2021
Accepted manuscript online: July 22, 2021
Version of record online: ■■, ■■■

# FULL PAPER

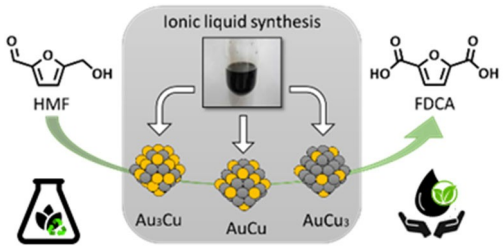


**Au/Cu nanoparticles** with different compositions and solid-solution type structures are obtained by chemical reduction in ionic liquids and supported on carbon. Annealing led to nanoparticles of the ordered intermetallic $L1_0$ AuCu phase. The effect of Cu addition and intermetallic structure on the catalytic performance is evaluated in the of the biomass-derived platform molecule, 5-hydroxymethyl-2-furfural, to 2,5-furandicarboxylic acid.

*G. Uzunidis, Dr. O. Schade, Dr. D. Schild, Prof. Dr. J.-D. Grunwaldt, Prof. Dr. S. Behrens**